

Article

Ionic Conductivity of LiSiON and the Effect of Amorphization/Heterovalent Doping on Li⁺ Diffusion

Siyuan Wu^{1,2}, Ruijuan Xiao^{1,2,*} , Hong Li^{1,2,*} and Liquan Chen^{1,2}

¹ Beijing Advanced Innovation Center for Materials Genome Engineering, Institute of Physics, Chinese Academy of Sciences, Beijing 100190, China; wusiyuan18@mails.ucas.ac.cn (S.W.); lqchen@iphy.ac.cn (L.C.)

² School of Physical Sciences, University of Chinese Academy of Sciences, Beijing 100190, China

* Correspondence: rjxiao@iphy.ac.cn (R.X.); hli@iphy.ac.cn (H.L.)

Abstract: The search for and design of suitable superior lithium ion conductors is a key process for developing solid state batteries. In order to realize a large range of applications, we researched the ionic conductivity of LiSiON, an example oxynitride mainly composed of elements with high abundance and a similar mixed anion size. Both its amorphous and heterovalent-doped phases were studied through density functional theory simulations. The Li⁺ ion diffusion behaviors and related properties are discussed. These elements are abundant in nature, and we found that amorphization or doping with P obviously enhanced the ionic conductivity of the system. General strategies to improve the kinetic properties of a candidate structure are presented, to help in the design of solid state electrolytes for lithium batteries.

Keywords: fast ion conductor; solid state lithium battery; density functional theory simulations



Citation: Wu, S.; Xiao, R.; Li, H.; Chen, L. Ionic Conductivity of LiSiON and the Effect of Amorphization/Heterovalent Doping on Li⁺ Diffusion. *Inorganics* **2022**, *10*, 45. <https://doi.org/10.3390/inorganics10040045>

Academic Editors: Christian Julien and Alain Mauger

Received: 28 February 2022

Accepted: 24 March 2022

Published: 31 March 2022

Publisher's Note: MDPI stays neutral with regard to jurisdictional claims in published maps and institutional affiliations.



Copyright: © 2022 by the authors. Licensee MDPI, Basel, Switzerland. This article is an open access article distributed under the terms and conditions of the Creative Commons Attribution (CC BY) license (<https://creativecommons.org/licenses/by/4.0/>).

1. Introduction

With the rapidly increasing requirements for clean energy, to reduce carbon emissions, using electric vehicles (EV), or even electric flights, is one of the main methods of realizing carbon neutrality [1–3]. In order to enhance the safety and energy density, solid state batteries have higher requirements [4–7]. A few solid-state electrolytes, such as Li₁₀GeP₂S₁₂ [8], Li_{9.54}Si_{1.74}P_{1.44}S_{11.7}Cl_{0.3} [9], and even β-Al₂O₃ [10], show comparable ionic conductivities with liquid electrolytes, while some commonly used lithium ion electrolytes, such as Li₇La₃Zr₂O₁₂ [11], Li_{3x}La_{2/3-x}TiO₃ [12], and Li₂O-Al₂O₃-GeO₂-P₂O₅ [13] provide 0.1–1 mS/cm, which almost meets the requirements for EVs. However, the key purpose of using solid-state batteries is to replace the millions of fuel vehicles, and it is necessary to use abundant elements in the Earth to lower the cost and accelerate electrification. As such, use of some rare elements, such as Ge in LGPS/LAGP, La in LLZO/LLTO, will hinder this process. Using cheaper and more abundant elements will also promote EVs from the perspective of economy. Si is the second richest element in the Earth's crust, and there are almost endless applications, thanks to glass and chip. SiO₂ is so common that it is not affected by the rising price of raw materials. In addition, using Si to substitute P in sulfides can also improve stability and ionic conductivity, such as in Li_{9.54}Si_{1.74}P_{1.44}S_{11.7}Cl_{0.3} [9] and Li₂SiS₃ [14].

Cation doping is a powerful method to improve ionic conductivity, by enhancing the concentration of the carrier, such as Li₁₀GeP₂S₁₂ [8], Li_{9.54}Si_{1.74}P_{1.44}S_{11.7}Cl_{0.3} [9], Li₇La₃Zr₂O₁₂ [11], and Li_{3x}La_{2/3-x}TiO₃ [12]. Besides cation doping, utilizing mixed anions is also an effective way to increase the ionic conductivity. Using O to partially replace S gives an improvement of both the ionic conductivity and the stability in a Li₃PS₄ system [15,16]. The new oxysulfide material LiAlSO, and some of its derivatives in ABXO form (A, B = Metals; X = S, Se, and Te), have been suggested as fast ion conductors by high-throughput calculations [17,18]. Besides S²⁻ ions, N³⁻ and F⁻ ions can also coexist

with O^{2-} , because of the close ionic size between them, to form oxynitrides and oxyfluorides, respectively. Apart from doping, amorphization is another method to enhance ion diffusion [19–22].

In this article, we chose LiSiON [23], mainly composed of elements with high abundance, as an example oxynitride, to discuss the kinetic properties of a material with a similar mixed anion size. An attempt to improve the Li^+ ion diffusion was made, by creating various chemical environments, including crystal, amorphous, and doped structures. With amorphization or doping with P, the diffusion coefficient of Li^+ was enhanced by orders of magnitude. Compared with oxysulfides, the similar ion radius and more carriers created by heterovalent doping represent a method to design suitable solid state electrolytes for batteries.

2. Results

2.1. The Crystal Structure and Basic Properties of α -LiSiON

The crystal structure of α -LiSiON belongs to the Pca21 space group in the orthorhombic system [23]. Figure 1a shows the lattice structure of α -LiSiON after geometrical relaxation. The optimized lattice parameters are $a = 5.233 \text{ \AA}$, $b = 6.410 \text{ \AA}$, and $c = 4.784 \text{ \AA}$, which are slightly overestimated by $\sim 0.9\%$ maximum compared with the experimental values. The unit cell contains four formula units (f.u.), with 16 ions in total. Each Li^+ ion coordinates three O^{2-} ions with a Li-O bond length of 1.92, 1.93, and 2.05 \AA , and one N^{3-} ion with the Li-N bond length of 2.25 \AA . Each Si^{4+} ion coordinates one O^{2-} ion with a Si-O bond length of 1.63 \AA , and three N^{3-} ions with a Si-N bond length of 1.73, 1.74, and 1.78 \AA . Distorted LiO_3N and $SiON_3$ tetrahedrons are connected in a vertex-sharing manner by O^{2-} or N^{3-} ions. LiO_3N tetrahedrons form a connected network in the ac -plane, and the neighboring LiO_3N planes are separated by $SiON_3$ tetrahedrons in the b direction, which implies that the lithium diffusion pathways potentially exist in the ac -plane with a two-dimensional form.

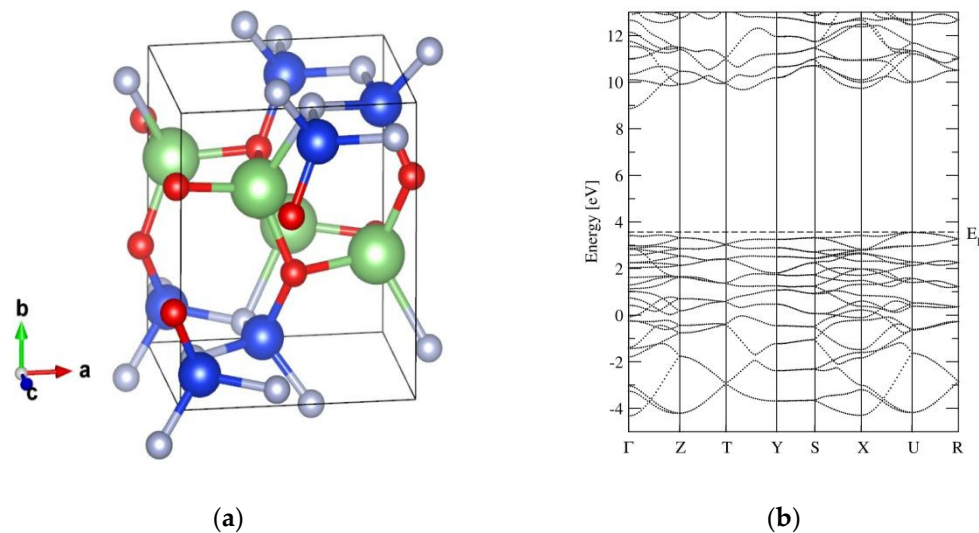


Figure 1. (a) The crystal structure and (b) the band structure of α -LiSiON. The green, blue, red, and gray spheres represent Li, Si, O, and N atoms, respectively.

Before investigating the kinetic properties of the LiSiON system, we first made a basic investigation of its thermostability and band structures. To date, α -LiSiON has been experimentally synthesized by solid state reactions. To check the stability of α -LiSiON, the formation energy with respect to its stable constituent phases was estimated according to the following two possible reactions:



By performing DFT calculations for the related compounds, the reaction energies of -0.672 eV/f.u. and -0.191 eV/f.u. were evaluated for Equations (1) and (2), respectively, indicating that LiSiON is intrinsically thermodynamically stable at 0 K. Previous studies reported that the thermal decomposition of LiSiON happens at 1300 °C, resulting in the formation of Li_2SiN_2 and probably amorphous SiO_2 [24]. The decomposition condition is far beyond the operational temperature of lithium batteries; thus, we believe α -LiSiON is promisingly stable within the temperature range, when working as a solid state electrolyte.

The band structure of α -LiSiON is presented in Figure 1b. To be used as an electrolyte, a wide band gap should be maintained, to ensure negligible electronic conductivity. It is obvious that the α -LiSiON phase shows characteristics of a wide-band-gap insulator, with a band gap of ~ 5 eV, which is comparable to the band gaps of a crystalline Li-P-O-N system [25], ensuring the wide electrochemical window of this material.

2.2. Ionic Diffusion Properties of α -LiSiON

After obtaining a preliminary understanding of the thermostability and electronic structure of α -LiSiON, we started to investigate its ionic transport properties with both the quasiempirical bond-valence (BV) method [26] and DFT-based nudged-elastic band (NEB) method [27]. The former gave us initial knowledge of the diffusion channels and directions in the structure, and the latter provided a more accurate evaluation of the energy barrier for each pathway. Figure 2 illustrates the isosurfaces of the potential energies calculated using the BV-based method, in which the preferred diffusion channels viewed in ab -, ac -, and bc -planes are given. The continuous pathways are formed in a zigzag pattern in ac -plane.

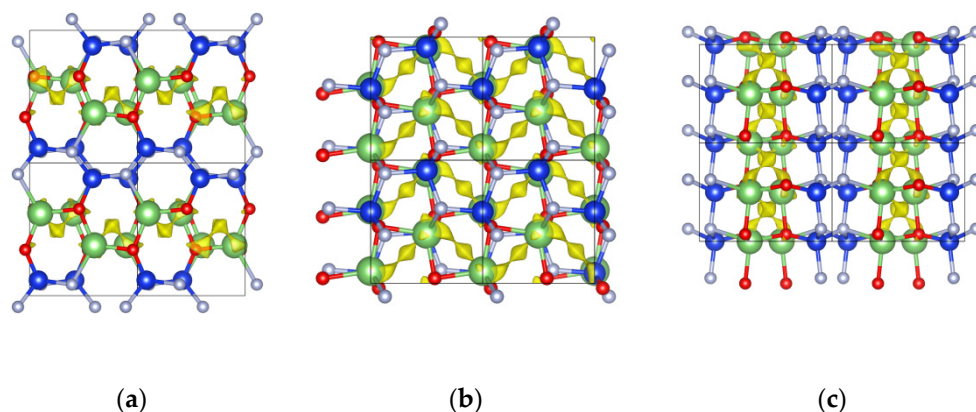


Figure 2. The Li^+ diffusion pathways evaluated using the bond valence method and represented by yellow isosurfaces, with the isovalue of 0.90 eV, viewed in the (a) ab -, (b) ac -, and (c) bc -plane. The green, blue, red, and gray spheres represent Li, Si, O, and N atoms, respectively.

Based on the Li^+ ion diffusion pathways revealed by the BV method, DFT simulations of the kinetic properties were performed using transition-state theory and the NEB method [27]. The hopping events of Li^+ ions from one lattice site to the neighboring one, assisted by the vacancy along $[110]$ and $[100]$, were considered, and the calculated barrier shapes and corresponding activation energies are shown in Figure 3. Along the $[110]$ direction, the vacancy hopping was the migration with the lower barrier of ~ 0.13 eV, while the energy barrier for Li^+ hopping along the $[100]$ direction was about 0.36 eV. Thus, as predicted by the BV method, a zigzag transporting network could be formed in the ac plane, with a very low energy barrier of ~ 0.13 eV, as shown in Figure 3a.

Besides the energy barrier, the formation energy of carriers also plays a role in determining the ionic conductivity; since, the latter correlates with the carrier concentration in the structure. To further understand the diffusion behavior in α -LiSiON, ab initio molecular dynamics (AIMD) simulations at 10 temperatures, ranging from 1600 K to 2600 K, were performed, with the parameters described in Section 4. Mean squared displacements (MSD), as indicated in Figures 4a and S1, were adopted to measure the deviation of ions over

time, with respect to their initial positions. The whole structural framework constituted by SiON was stable, since the MSDs of Si, O, and N remained less than 2 \AA^2 , even at 2600 K. However, hopping events of Li^+ ions appeared frequently until reaching high temperature, and MSDs with values larger than 100 \AA^2 were only exhibited at 2500 K and 2600 K. While for solid electrolytes with comparable activation energies, e.g., the E_a of $0.21 \pm 0.01 \text{ eV}$ in $\text{Li}_{10}\text{GeP}_2\text{S}_{12}$ and the E_a of $0.25 \pm 0.02 \text{ eV}$ in $\text{Li}_{1.33}\text{Al}_{0.33}\text{Ti}_{1.67}(\text{PO}_4)_3$ [28], much lower temperatures were needed to induce Li^+ ion hopping. Since similar E_a values are found among these systems, this implies that the formation of carriers in α -LiSiON is much more difficult, because of the full occupation of Li^+ at the lattice sites. The Li^+ ion diffusion energy barrier extracted from the Arrhenius plot of diffusion coefficients, as shown in Figure 4b, was $1.59 \pm 0.24 \text{ eV}$. The E_a values obtained from AIMD represent the self-diffusion process, in which the energies for creating carriers are included. When taking E_a as the summation of the energy barrier and half the formation energy of the Li vacancy, we can estimate that the energy for creating the Li vacancy is around 3 eV , which is ~ 20 times larger than the energy barrier of 0.13 eV . Therefore, decreasing the formation energy of the Li^+ vacancy or enhancing the vacancy concentrations were the subsequent procedures aimed at improving the ionic conductivities of the LiSiON system. Creating a frustrated energy landscape [29] and heterovalent ion doping [30] have been proven to be promising strategies in other fast ion conductors. In the following, the two methods, including amorphization of the structure and element doping, were attempted for the LiSiON system.

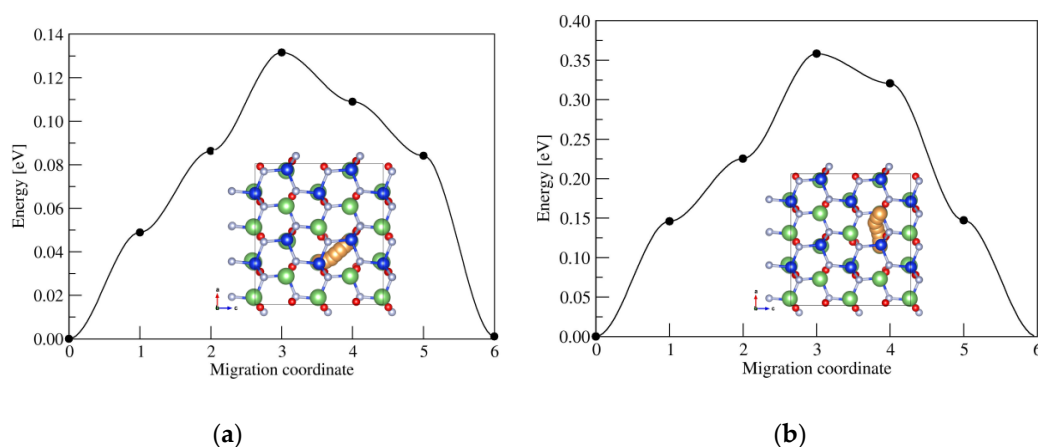


Figure 3. The Li^+ diffusion energy barriers of (a) the inline migration mode, and (b) the interline migration model simulated by the NEB method.

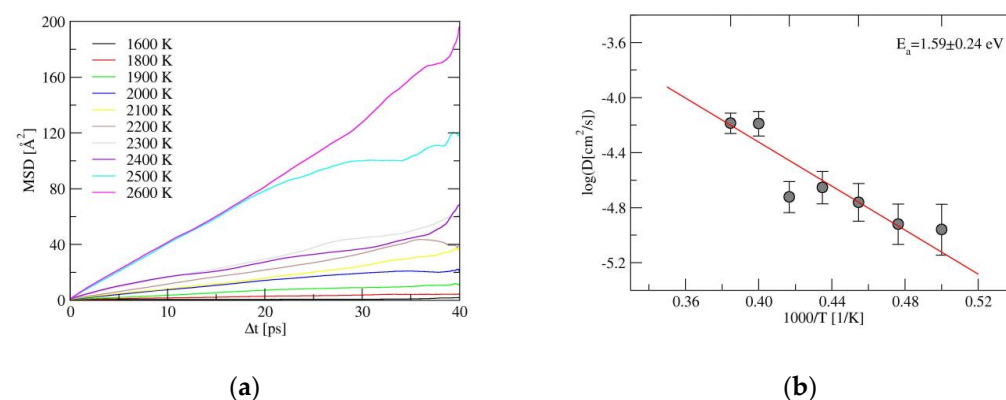


Figure 4. (a) The mean-squared-displacements (MSD) for Li^+ ions simulated by AIMD, and (b) the Arrhenius plot of diffusion coefficients for α -LiSiON, from which the Li^+ ion diffusion energy barrier was obtained, with the error bars of $\log D$ given as vertical lines.

2.3. The Properties of Amorphous-LiSiON

To model the effect of amorphization of LiSiON on the Li⁺ ion diffusion, an atomic structure of amorphous-LiSiON was built by simulating the quenching process, as described in the Method Section. After melting and quenching, the disordered structure was frozen at 300 K, as illustrated in Figure 5a. The coordination analysis indicated that Si⁴⁺ ions remained in the four coordinate environments, but, besides the SiON₃ tetrahedron, SiO₂N₂ and SiON₃ tetrahedrons were also found in the amorphous structure. Zanotto et al. used NMR measurement and found similar structures, such as SiO₃N, SiO₂N₂, and SiON₃ in nitrated lithium disilicate glasses [31]. Unlike the crystal phase, in which all the SiON₃ polyhedrons are connected by vertexes, both vertex-shared and edge-shared connections appear. The coordination environment of Li⁺ ions in an amorphous structure is much more complex than that in a crystal, since 3-, 4-, and 5-coordinated Li⁺ are observed in the disordered structure. The partial radial distribution function (PRDF) for Li-O, Li-N, Si-O, and Si-N pairs in amorphous-LiSiON can be seen in Figure S2, and all pairs became wider, indicating the varied distribution of bond lengths in the amorphous state. The coexistence of O and N and the various distortions of each polyhedron offer no regular sites for Li ions, which creates a frustrated environment, similar to that in the superionic conductor LiTi₂(PS₄)₃ [29].

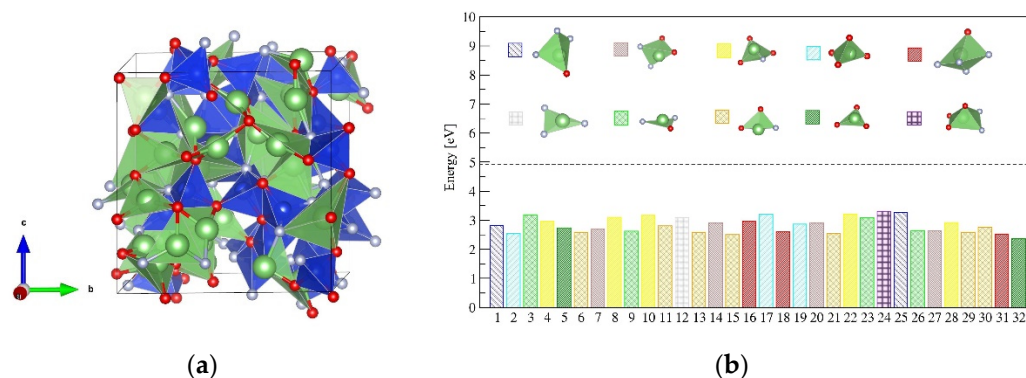
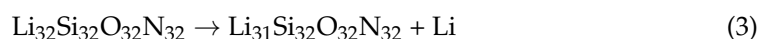


Figure 5. (a) The disordered structure of amorphous-LiSiON frozen at 300 K, in which the green, blue, red, and gray spheres represent Li, Si, O, and N atoms, respectively. (b) The formation energy for each of the Li vacancy in amorphous-LiSiON and the coordination environment of each Li site. The value for creating one Li vacancy in crystalline α -LiSiON is indicated as a horizontal dotted line for comparison.

The coordination environments for the 32 Li sites in the disordered structure are illustrated in Figure 5b. Ten types of chemical environments, including 3-coordinated LiN₃, LiON₂, LiO₂N, LiO₃, 4-coordinated LiON₃, LiO₂N₂, LiO₃N, LiO₄, and 5-coordinated LiON₄, LiO₃N₂, were observed. The formation energies for creating Li vacancies in these environments were estimated in the cell with 32 f.u., according to Equations (3) and (4),



$$E_{f(\text{Li_vacancy})} = E(\text{Li}_{31}\text{Si}_{32}\text{O}_{32}\text{N}_{32}) + E(\text{Li}) - E(\text{Li}_{32}\text{Si}_{32}\text{O}_{32}\text{N}_{32}) \quad (4)$$

The formation energy for each of the Li vacancies in amorphous-LiSiON is given in Figure 5b. The $E_{f(\text{Li_vacancy})}$ values varied among the 32 sites, because of the diverse coordination environments; however, all of them were around 3 eV and much lower than the $E_{f(\text{Li_vacancy})}$ value in crystalline α -LiSiON. Thus, the carrier concentration in amorphous-LiSiON is much higher than that in the crystal phase.

The results of the AIMD simulations for amorphous-LiSiON are shown in Figure 6. Compared with α -LiSiON, much lower temperatures were needed to observe the Li⁺ ion diffusion. For the nine simulation temperatures, the data from those larger than 800 K were adopted to obtain the diffusion coefficients and the activation energy. As indicated

in Figure 6b, the evaluated E_a for amorphous-LiSiON was 0.18 ± 0.08 eV, which is very close to the energy barriers estimated using the NEB method in α -LiSiON, indicating that amorphization effectively decreased the energies needed for carrier creation.

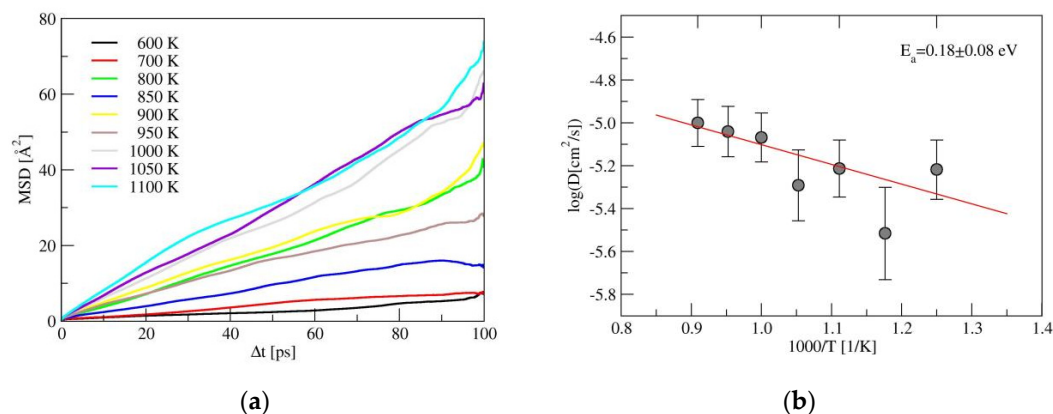


Figure 6. (a) The MSD for Li^+ ions simulated by AIMD, and (b) Arrhenius plot of diffusion coefficients for amorphous-LiSiON.

Along with the disordering process, the band gap of the LiSiON system changes from ~ 5 eV in crystal phase, to ~ 3 eV in amorphous states. The density of states for α -LiSiON and amorphous-LiSiON are compared in Figure 7. Referring to the Fermi level (E_F), the electronic states of α -LiSiON, ranging from -2 to 0 eV, are mainly occupied by O $2p$ and N $2p$ orbitals, with nearly no contribution from Li and Si, indicating that the states from O and N dominate the valence band of α -LiSiON. The electronic states ranging from -8 to -2 eV illustrate the covalent characteristics of Si-O and Si-N chemical bonds, because of the orbital hybridization between Si $3p$ and O $2p$ states, and between Si $3p$ and N $2p$ states. In amorphous phase, both the p states of O and N are dispersed in a broader range, reflecting the diversified strength of bond interactions in the disordered state. The diversity of bond characteristics in the amorphous phase were also confirmed by the Bader charge analysis. The calculated Bader charges of O and N in α -LiSiON were -1.62 e and -2.26 e, respectively, while those in amorphous-LiSiON for O were distributed in the range of $-1.66 \sim -1.57$ e, and the charge for N was distributed from -2.30 to -2.14 e.

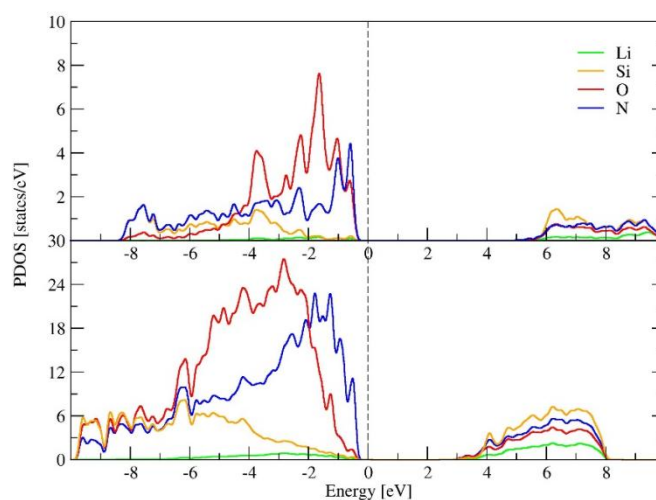
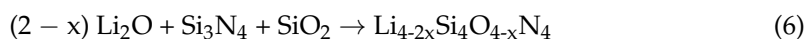


Figure 7. The density of states for α -LiSiON (upper panel) and amorphous-LiSiON (lower panel).

2.4. Ionic Diffusion Properties of P-Doped α -LiSiON

Besides adjusting the formation energies of carriers, another way to improve the carrier concentrations is to introduce vacancies by doping with heterovalent ions. For

example, Equation (5) demonstrates using a higher valence state P^{5+} to replace part of Si^{4+} , to introduce Li vacancies; and Equation (6) shows the substitution of N^{3-} with O^{2-} to create Li vacancies in the structure. We adopted the method of a P-doped Si site, to investigate manners of improving the ionic conductivity.



The doping is simulated in the primitive cell with 4 f.u., in which one, two, or three of the four Si sites is(are) replaced by P, and one, two, or three of the four Li ions is(are) removed. More details are shown in Tables S1–S3, and we found that 0.25 is the best P content to obtain the lowest Li^+ migration energy barrier using the BV method; therefore, subsequently, we only considered $Li_{0.75}Si_{0.75}P_{0.25}ON$ by AIMD. Sixteen configurations were constructed to simulate Si/P and Li/vacancy coexistence. The total energies of these structures and the Li^+ ion diffusion barrier evaluated using the BV method are listed in Table S1. The structure with the lowest total energy was regarded as the most stable and selected to further investigate the Li^+ ion diffusion properties with the AIMD technique in the P-doped LiSiON system. The MSD of Li^+ ions simulated using AIMD for P-doped LiSiON is shown in Figure 8, and a similar Li^+ ion diffusion ability was found compared to amorphous-LiSiON, indicating that creating Li vacancies in advance by heterovalent ion doping is also an effective way to optimize the kinetic properties within a candidate structural framework. The ion conductivity for P doping by extrapolation to the room temperature was 3.9×10^{-3} mS/cm. The effectiveness of P doping could be confirmed by comparing it to the 2.5×10^{-20} mS/cm in a crystal LiSiON.

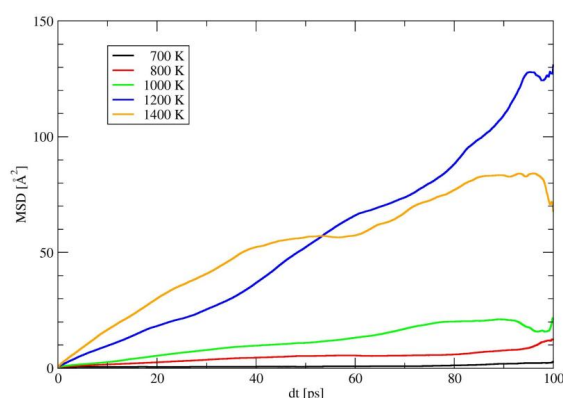


Figure 8. The MSD for Li^+ ions simulated by AIMD for P-doped LiSiON.

3. Discussion and Conclusions

We chose LiSiON as an example of oxynitride, in order to discuss the superionic kinetic properties of materials with a similar mixed anion size. Si is the second richest element in the Earth's crust and may be suitable for large-scale applications in batteries. Besides the approximate radius between O^{2-} and N^{3-} , Si is also easier to be doped with P, which provides a large chemical space for Li-Si-O-N to investigate. Although LiSiON has a small migration energy barrier, the large formation energy of the Li vacancy is the rate limitation for self-diffusion of Li in LiSiON. Amorphization and doping to create carriers have been proven to be good choices for improving ionic conductivity. Some experiments [32–34] revealed that the similar components or amorphization in the Li-Si-P-O-N chemical space will enhance the ionic conductivity, which is consistent with our theoretical prediction for the LiSiON system. In Table S4, we calculated that the ion conductivities for crystal/amorphous/P-doped are 2.5×10^{-20} , 8.1 and 3.9×10^{-3} mS/cm, respectively, by extrapolation to room temperature. It is evident that doping and amorphization can enhance ion conductivity.

Combined with other possible strategies, such as introducing concerted migration [35] and dynamic coupling [36–39], the methods for improving the ionic conductivity for a candidate framework are summarized in Figure 9. Meanwhile, the Li^+ concentrations can be adjusted by heterovalent doping, and may be suitable for the different sides in batteries. According to the space charge interface model [40–42], they may match the cation/anode with suitable doping, as shown in the first column of Figure 9. The creation of a vacancy (upper panel) and interstitial (lower panel) will provide Li-poor and Li-rich samples. Moreover, they may be suitable for the cation or anode sides, respectively. In addition, the Li^+ concentrations may affect the electrochemical stability window [43,44], and the combination of different concentrations for the two sides may be a good choice to enlarge the electrochemical window.

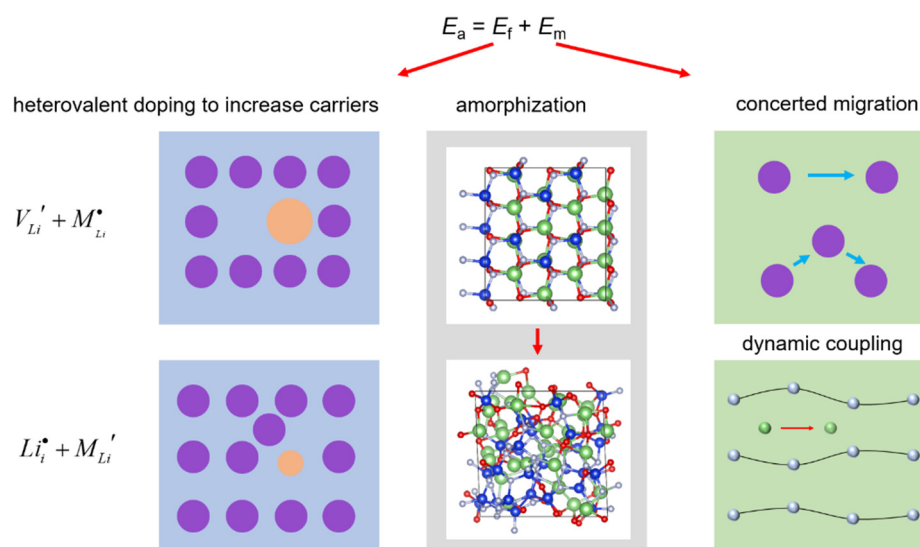


Figure 9. Strategies to improve the ionic conductivity for a candidate framework.

In summary, we have discussed the ionic conductivity of LiSiON . Vacancy-assisted Li^+ diffusion in LiSiON is improved by amorphization or by doping P^{5+} to form a Li-poor material. In addition, amorphization will reduce the E_a for diffusion, due to the abundant coordination, while heterovalent doping will provide Li vacancies in advance. Both of these increase the carrier concentration in the structure and effectively improve the Li^+ diffusion behavior. We hope our work will be helpful for designing solid state electrolytes for lithium batteries.

4. Materials and Methods

4.1. DFT-Based Structural Relaxation and Band Structure Calculations

The present calculations were performed with the Vienna ab initio simulation package (VASP) [45] using the generalized gradient approximation, with a parameterized exchange–correlation functional according to Perdew–Burke–Ernzerhof [46]. The cutoffs for the wavefunction and density were 500 eV and 756 eV, respectively. For the crystal structure optimization and the electronic structure evaluation, the k-mesh used to sample the Brillouin zone was $10 \times 8 \times 11$ for the conventional cell, and $5 \times 5 \times 5$ for the supercell. In both cases, the Γ point was included. The non-spin-polarized scheme was adopted for all the simulations in this work. Both ions and cells was relaxed in the optimization, with the energy and force convergence criterions of 10^{-5} eV and 0.01 eV/Å, respectively.

4.2. BV and NEB Simulations

Both the semi-empirical bond valence (BV) method and accurate quantum mechanical calculations based on density functional theory (DFT) were adopted to understand the kinetic properties of α - LiSiON . The initial estimation of the Li^+ ion diffusion pathways

utilized BV calculations [15,26], in which the Li^+ ions were assumed to move within the framework composed of immobile anions and cations. The interactions between a dummy Li^+ ion in the space and the ions around it were empirically evaluated by summation of the attraction between Li^+ and anions described by the Morse-type potential and the repulsion between Li^+ and cations expressed by the Coulombic potential. Maps of the total potential energy, $E(\text{Li})$, on grids of points with a resolution of 0.1 \AA were built in the unit cell. Then, the threshold value of $E(\text{Li})$ to form a continuous pathway was estimated as the Li^+ migration energy barrier. The energy barriers of the typical pathways found in the BV simulations were calculated using the NEB method [27], with the energy and force convergence criterions of 10^{-5} eV and 0.02 eV/\AA , respectively.

4.3. The Model Building of Amorphous-LiSiON

To create the amorphous structure of LiSiON, we started from the crystalline α -LiSiON lattice in a $2 \times 2 \times 2$ supercell, with 128 atoms in total. The ab initio molecular dynamics (AIMD) method was adopted to build the atomic position for the disorder phase. First, the ensemble was melted at 3000 K and allowed to equilibrate at this temperature for 20 ps with a timestep of 2 fs. The system was then quenched to room temperature at a rate of 1 K per timestep. We subsequently relaxed the atomic coordinates and length of the cell lattice with an atomic force tolerance of 0.01 eV/\AA . The molecular dynamics calculations were carried out on the Γ point to equilibrate the computational cost and the accuracy.

4.4. The AIMD Simulations

The kinetic properties of Li^+ ion diffusion were studied using the AIMD method. The simulations were performed on a $2 \times 2 \times 2$ supercell containing 32 formula units (128 atoms in total), and only the Γ point was used for Brillouin zone sampling. The AIMD run was carried out with a Nose thermostat for 40,000 steps, with a time step of 1 fs. No obvious Li migration was observed in the simulations with temperatures of 1600 and 1800 K. To keep the computational cost at a reasonable level, we raised the temperature to increase the possibility of Li ion diffusion; and the results of the latter were used to investigate the diffusion pathways. The kinetic properties were extracted using the molecular dynamics analysis package developed by Mo et al. [28].

Supplementary Materials: The following supporting information can be downloaded at: <https://www.mdpi.com/article/10.3390/inorganics10040045/s1>, Figure S1: The mean-squared-displacements (MSD) for Li^+ , Si^{4+} , O^{2-} , and N^{3-} ions simulated by AIMD; Figure S2: The partial radial distribution function (PRDF) for Li-O, Li-N, Si-O, and Si-N pairs in amorphous-LiSiON; Tables S1–S3: The total energies (E_{tot}) of 16/12/4 configurations for $\text{Li}_{0.75}\text{Si}_{0.75}\text{P}_{0.25}\text{O}_4/\text{Li}_{0.5}\text{Si}_{0.5}\text{P}_{0.5}\text{O}_4/\text{Li}_{0.25}\text{Si}_{0.25}\text{P}_{0.75}\text{O}_4$ and the Li^+ ion diffusion barriers evaluated using the BV method (E_a by BV); Table S4: The estimated value for the ionic conductivities at 300 K for crystal α -LiSiON, amorphous-LiSiON and P-doped LiSiON ($\text{Li}_{0.75}\text{Si}_{0.75}\text{P}_{0.25}\text{O}_4$) according to the Arrhenius plot of diffusion coefficients.

Author Contributions: Conceptualization, R.X. and H.L.; validation, S.W. and R.X.; investigation, S.W. and R.X.; data curation, S.W. and R.X.; writing—original draft preparation, S.W. and R.X.; writing—review and editing, R.X. and H.L.; supervision, H.L. and L.C. All authors have read and agreed to the published version of the manuscript.

Funding: This research was funded by the National Natural Science Foundation of China (grant number 52022106 and 52172258) and the Informatization Plan of Chinese Academy of Sciences (grant number CAS-WX2021SF-0102).

Data Availability Statement: Data available on request.

Acknowledgments: We acknowledge the Tianjin Supercomputer Center for providing computing resources.

Conflicts of Interest: The authors declare no conflict of interest.

References

1. Armand, M.; Tarascon, J.M. Building better batteries. *Nature* **2008**, *451*, 652–657. [[CrossRef](#)] [[PubMed](#)]
2. Goodenough, J.B.; Kim, Y. Challenges for Rechargeable Li Batteries. *Chem. Mater.* **2010**, *22*, 587–603. [[CrossRef](#)]
3. Viswanathan, V.; Epstein, A.H.; Chiang, Y.; Takeuchi, E.; Bradley, M.; Langford, J.; Winter, M. The challenges and opportunities of battery-powered flight. *Nature* **2022**, *601*, 519–525. [[CrossRef](#)]
4. Hu, Y. Batteries: Getting solid. *Nat. Energy* **2016**, *1*, 16042. [[CrossRef](#)]
5. Janek, J.; Zeier, W. A solid future for battery development. *Nat. Energy* **2016**, *1*, 16141. [[CrossRef](#)]
6. Balaish, M.; Gonzalez-Rosillo, J.; Kim, K.; Zhu, Y.; Hood, Z.; Rupp, J.M. Processing thin but robust electrolytes for solid-state batteries. *Nat. Rev. Mater.* **2020**, *5*, 229. [[CrossRef](#)]
7. Xu, L.; Lu, Y.; Zhao, C.; Yuan, H.; Zhu, G.; Hou, L.; Zhang, Q.; Huang, J. Toward the Scale-Up of Solid-State Lithium Metal Batteries: The Gaps between Lab-Level Cells and Practical Large-Format Batteries. *Adv. Energy Mater.* **2020**, *11*, 2002360. [[CrossRef](#)]
8. Kamaya, N.; Homma, K.; Yamakawa, Y.; Hirayama, M.; Kanno, R.; Yonemura, M.; Kamiyama, T.; Kato, Y.; Hama, S.; Kawamoto, K.; et al. A lithium superionic conductor. *Nat. Mater.* **2011**, *10*, 682–686. [[CrossRef](#)]
9. Kato, Y.; Hori, S.; Saito, T.; Suzuki, K.; Hirayama, M.; Mitsui, A.; Yonemura, M.; Iba, H.; Kanno, R. High-power all-solid-state batteries using sulfide superionic conductors. *Nat. Energy* **2016**, *1*, 16030. [[CrossRef](#)]
10. Bates, J.; Engstrom, H.; Wang, J.; Larson, B.; Dudney, N.; Brundage, W. Composition, ion-ion correlations and conductivity of beta"-alumina. *Solid State Ionics* **1981**, *5*, 159–162. [[CrossRef](#)]
11. Murugan, R.; Thangadurai, V.; Weppner, W. Fast Lithium Ion Conduction in Garnet-Type Li₇La₃Zr₂O₁₂. *Angew. Chem. Int. Ed.* **2007**, *46*, 7778–7781. [[CrossRef](#)] [[PubMed](#)]
12. Inaguma, Y.; Chen, L.; Itoh, M.; Nakamura, T.; Uchida, T.; Ikuta, H.; Wakihara, M. High ionic conductivity in lithium lanthanum titanate. *Solid State Commun.* **1993**, *86*, 689–693. [[CrossRef](#)]
13. Fu, J. Fast Li⁺ ion conducting glass-ceramics in the system Li₂O–Al₂O₃–GeO₂–P₂O₅. *Solid State Ionics* **1997**, *10*, 191–194. [[CrossRef](#)]
14. Huang, W.; Matsui, N.; Hori, S.; Suzuki, K.; Hirayama, M.; Yonemura, M.; Saito, T.; Kamiyama, T.; Sasaki, Y.; Yoon, Y.; et al. Anomalously High Ionic Conductivity of Li₂SiS₃-Type Conductors. *J. Am. Chem. Soc.* **2022**, *144*, 4989–4994. [[CrossRef](#)] [[PubMed](#)]
15. Xiao, R.; Li, H.; Chen, L. High-throughput design and optimization of fast lithium ion conductors by the combination of bond-valence method and density functional theory. *Sci. Rep.* **2015**, *5*, 14227. [[CrossRef](#)]
16. Wang, X.; Xiao, R.; Li, H.; Chen, L. Oxygen-driven transition from two-dimensional to three-dimensional transport behaviour in β-Li₃PS₄ electrolyte. *Phys. Chem. Chem. Phys.* **2016**, *18*, 21269–21277. [[CrossRef](#)]
17. Wang, X.; Xiao, R.; Li, H.; Chen, L. Oxysulfide LiAlSO: A Lithium Superionic Conductor from First Principles. *Phys. Rev. Lett.* **2017**, *118*, 195901. [[CrossRef](#)]
18. He, J.; Yao, Z.; Hegde, V.; Naghavi, S.; Shen, J.; Bushick, K.; Wolverton, C. Computational Discovery of Stable Heteroanionic Oxychalcogenides ABXO (A, B = Metals; X = S, Se, and Te) and Their Potential Applications. *Chem. Mater.* **2020**, *32*, 8229–8242. [[CrossRef](#)]
19. Angell, C.A. Mobile Ions in Amorphous Solids. *Annu. Rev. Phys. Chem.* **1992**, *43*, 693–717. [[CrossRef](#)]
20. Bates, J.B.; Dudney, N.J.; Gruzalski, G.R.; Zuhr, R.A.; Choudhury, A.; Luck, C.F.; Robertson, J.D. Fabrication and characterization of amorphous lithium electrolyte thin films and rechargeable thin-film batteries. *J. Power Source* **1993**, *43*, 103–110. [[CrossRef](#)]
21. Takuya, K.; Chie, H.; Atsushi, S.; Akitoshi, H.; Masahiro, T. Mechanochemical synthesis and characterization of amorphous Li₂CN₂ as a lithium ion conductor. *J. Ceram. Soc. Jpn.* **2019**, *127*, 518–520.
22. Minami, T.; Hayashi, A.; Tatsumisago, M. Recent progress of glass and glass-ceramics as solid electrolytes for lithium secondary batteries. *Solid State Ionics* **2006**, *177*, 2715–2720. [[CrossRef](#)]
23. Laurent, Y.; Guyader, J.; Roult, G. Etude par diffraction de neutrons selon la method du temps de vol de LiSiON α . *Acta Cryst.* **1981**, *37*, 911–913. [[CrossRef](#)]
24. Podsiadlo, S. Formation and Thermal Decomposition of Silicon Oxynitride Compounds II. *J. Therm. Anal.* **1987**, *32*, 445–449. [[CrossRef](#)]
25. Du, Y.A.; Holzwarth, N.A.W. First-principles study of LiPON and related solid electrolytes. *Phys. Rev. B* **2010**, *81*, 184106.
26. Adams, S.; Rao, R.P. High power lithium ion battery materials by computational design. *Phys. Status Solidi A* **2011**, *208*, 1746–1753. [[CrossRef](#)]
27. Henkelman, G.; Jónsson, H. Improved tangent estimate in the nudged elastic band method for finding minimum energy paths and saddle points. *J. Chem. Phys.* **2000**, *113*, 9978. [[CrossRef](#)]
28. He, X.; Zhu, Y.; Epstein, A.; Mo, Y. Statistical variances of diffusional properties from ab initio molecular dynamics simulations. *npj Comput. Mater.* **2018**, *4*, 18. [[CrossRef](#)]
29. Stefano, D.D.; Miglio, A.; Robeyns, K.; Filinchuk, Y.; Lechartier, M.; Senyshyn, A.; Ishida, H.; Spannenberger, S.; Prutsch, D.; Lunghammer, S.; et al. Superionic diffusion through frustrated energy landscape. *Chem* **2019**, *5*, 2450–2460. [[CrossRef](#)]
30. Xiao, R.; Li, H.; Chen, L.Q. High-throughput computational discovery of K₂CdO₂ as an ion conductor for solid-state potassium-ion batteries. *J. Mater. Chem. A* **2020**, *8*, 5157. [[CrossRef](#)]
31. Singh, S.P.; Schneider, J.F.; Kundu, S.; Rodrigues, A.C.M.; de Mattos, P.P.G.; Zanutto, E.D.; Rocherullé, J.; Bénard-Rocherullé, P.; Lebullenger, R. Structure and ionic conductivity of nitrated lithium disilicate (LiSiON) glasses. *Mater. Chem. Phys.* **2018**, *211*, 438–444. [[CrossRef](#)]

32. Famprakis, T.; Galipaud, J.; Clemens, O.; Pecquenard, B.; Le Cras, F. Composition Dependence of Ionic Conductivity in LiSiPO(N) Thin-Film Electrolytes for Solid-State Batteries. *ACS Appl. Energy Mater.* **2019**, *2*, 4782–4791. [[CrossRef](#)]
33. Lee, S.J.; Bae, J.H.; Lee, H.W.; Baik, H.K.; Lee, S.M. Electrical conductivity in Li–Si–P–O–N oxynitride thin-films. *J. Power Sources* **2003**, *123*, 61–64. [[CrossRef](#)]
34. Xia, Q.; Sun, S.; Zan, F.; Xu, J.; Xia, H. Amorphous LiSiON Thin Film Electrolyte for All-solid-state Thin Film Lithium Battery. *J. Inorg. Mater.* **2022**, *37*, 230–236. [[CrossRef](#)]
35. He, X.; Zhu, Y.; Mo, Y. Origin of fast ion diffusion in super-ionic conductors. *Nat. Comm.* **2017**, *8*, 15893. [[CrossRef](#)] [[PubMed](#)]
36. Zhang, Z.; Roy, P.N.; Li, H.; Avdeev, M.; Nazar, L.F. Coupled Cation–Anion Dynamics Enhances Cation Mobility in Room-Temperature Superionic Solid-State Electrolytes. *J. Am. Chem. Soc.* **2019**, *141*, 19360–19372. [[CrossRef](#)] [[PubMed](#)]
37. Zhang, Z.; Li, H.; Kaup, K.; Zhou, L.; Roy, P.N.; Nazar, L.F. Targeting Superionic Conductivity by Turning on Anion Rotation at Room Temperature in Fast Ion Conductors. *Matter* **2020**, *2*, 1667–1684. [[CrossRef](#)]
38. Zhang, Z.; Nazar, L. Exploiting the paddle-wheel mechanism for the design of fast ion conductors. *Nat. Rev. Mater.* **2022**, 1–17. [[CrossRef](#)]
39. Wu, S.; Xiao, R.; Li, H.; Chen, L. New insights into the mechanism of cation migration induced by cation–anion dynamic coupling in superionic conductors. *J. Mater. Chem. A* **2022**, *10*, 3093–3101. [[CrossRef](#)]
40. Morgan, B.J.; Madden, P.A. Effects of Lattice Polarity on Interfacial Space Charges and Defect Disorder in Ionically Conducting AgI Heterostructures. *Phys. Rev. Lett.* **2011**, *107*, 206102. [[CrossRef](#)]
41. Fu, L.; Chen, C.C.; Samuelis, D.; Maier, J. Thermodynamics of Lithium Storage at Abrupt Junctions: Modeling and Experimental Evidence. *Phys. Rev. Lett.* **2014**, *112*, 208301. [[CrossRef](#)]
42. Swift, M.; Qi, Y. First-Principles Prediction of Potentials and Space-Charge Layers in All-Solid-State Batteries. *Phys. Rev. Lett.* **2019**, *122*, 167701. [[CrossRef](#)] [[PubMed](#)]
43. Schwietert, T.K.; Vasileiadis, A.; Wagemaker, M. First-Principles Prediction of the Electrochemical Stability and Reaction Mechanisms of Solid-State Electrolytes. *J. Am. Chem. Soc.* **2021**, *143*, 1488–1496. [[CrossRef](#)] [[PubMed](#)]
44. Richards, W.D.; Miara, L.J.; Wang, Y.; Kim, J.C.; Ceder, G. Interface Stability in Solid-State Batteries. *Chem. Mater.* **2016**, *28*, 266–273. [[CrossRef](#)]
45. Kresse, G.; Furthmüller, J. Efficiency of ab-initio total energy calculations for metals and semiconductors using a plane-wave basis set. *Comput. Mater. Sci.* **1996**, *6*, 15–50.
46. Perdew, J.P.; Burke, K.; Ernzerhof, M. Generalized Gradient Approximation Made Simple. *Phys. Rev. Lett.* **1996**, *77*, 3865. [[CrossRef](#)]